

Synthesis of Titanium Dioxide/Cadmium Sulfide Nanosphere Particles for Photocatalyst Applications

Thi Thuy Duong Vu,^{†,‡} Frej Mighri,^{*,†,‡} Abdellah Ajji,^{‡,||} and Trong-On Do^{†,§}

[†]Department of Chemical Engineering, Laval University, Quebec, Quebec G1V 0A6, Canada

[‡]Center for Applied Research on Polymers and Composites (CREPEC); [§]Centre in Green Chemistry and Catalysis (CGCC);

^{||}Department of Chemical Engineering, École Polytechnique of Montreal, C.P. 6079, Montreal, Quebec H3C 3A7, Canada

ABSTRACT: Semiconductor nanocomposites, which are composed of titanium dioxide (TiO₂) nanorods, cadmium sulphide (CdS) nanoparticles (NPs), and Ni clusters, were synthesized. The following steps were adopted: (i) surfactant-capped TiO₂ nanorods with controlled length were synthesized in an autoclave using oleic acid and amino hexanoic acid as surfactants. By using a ligand-exchange procedure, in which nitrosonium tetrafluoroborate (NOBF₄) was used to replace the original surfactants, hydrophilic NOBF₄-TiO₂ nanorods were obtained; (ii) the resulting nanorods were deposited with CdS NPs and (iii) then deposited selectively with Ni clusters (as cocatalyst) on the nanocomposite surface. Under visible-light illumination of the nanocomposite, the generated electrons from the conduction band of CdS are transferred to TiO₂ via TiO₂/CdS interface, then to metallic Ni cluster. As a result, the electron–hole separation was highly enhanced, leading to a Ni–TiO₂/CdS nanocomposite with high photocatalytic performance for the production of hydrogen (H₂).

1. INTRODUCTION

As one of the most abundant elements with a high energy efficiency, hydrogen (H₂) generated via solar water splitting has currently attracted attention. Hydrogen energy yield is reported up to 122 kJ/g, which is largely higher than that of other fuels, such as gasoline (40 kJ/g).[†] So, H₂ is presently considered as one on the future ideal fuel candidates for the energy generation. Moreover, solar water splitting is environmentally friendly and has great potential for low-cost and clean hydrogen production. In addition, H₂ can be easily distributed over large distances through pipelines or via tankers. It can also be stored in gaseous, liquid, or metal hydride forms, thus providing a huge market potential.

In a photocatalytic H₂ production reaction from water, the chemical reaction is induced by photoirradiation in the presence of a photocatalyst. With a relative narrow band gap of 2.4 eV, CdS is one of the sulfide-based semiconductors, which have promising applications in photocatalysis.^{2–6} However, CdS alone shows very low H₂ generation rates due to the rapid recombination of photogenerated electrons and holes, which causes a lack of H₂ evolution sites. Good performances were mostly achieved in the presence of noble metal cocatalysts, such as platinum (Pt), palladium (Pd), and nickel (Ni). Among various strategies to improve the photocatalytic activity of CdS, the most efficient method is to promote the charge separation of photogenerated electrons and holes by coupling CdS with other semiconductors with adequate flat potentials, such as TiO₂,^{7,8} zinc oxide (ZnO),⁹ or graphene.^{10,11} In such systems, electrons from the conduction band of CdS can be transferred to other semiconductors or graphene, leading to improved electron–hole separation, which could enhance the generation rate of H₂. TiO₂ has been widely used as a photocatalyst due to its high photostability and oxidation efficiency, and its abundance and noncorrosives. It is also environmental friendly and cost-

effective.¹² With proper band structures, the TiO₂/CdS nanocomposite exhibits good properties in photocatalysis, leading to an improved photoproduction of H₂ under visible light.^{13–17}

Herein, we describe new non-noble metal–nanocomposites (NCs) as highly efficient and stable visible-light driven photocatalysts. These NCs are composed of TiO₂ nanorods, CdS NPs, and Ni clusters. An important advantage of TiO₂ nanorod-based nanocomposites is that CdS NPs are evenly dispersed on nanorod surface with strong bonding, and cocatalyst Ni clusters are selectively deposited on the surface of these nanorods. This configuration can improve the efficiency of electron transfer from the sensitized CdS NPs to TiO₂ and then to Ni clusters. As anticipated, Ni–TiO₂/CdS nanocomposites developed in the present work exhibit enhanced H₂ production from water under visible light using ethanol as a sacrificial reagent.

2. EXPERIMENTAL SECTION

2.1. Materials. All chemicals were used as received without further purification or distillation. Titanium(IV) butoxide (TB, 97%), oleic acid (OA, 90%), 6-aminohexanoic acid (6AHA), cadmium acetate dehydrate, thioamide, and nitrosonium tetrafluoroborate solution (NOBF₄) were purchased from Aldrich. Absolute ethanol, *N,N*-dimethylformamide (DMF), dichloromethane, hexane, and toluene, were, respectively, purchased from Brampton Canada, Fisher Scientific Canada, and Anachemia Canada. All of them were of analytical grade.

2.2. Synthesis of Length-Controlled TiO₂ Nanorods Using Oleic Acid and 6-Aminohexanoic Acid as

Received: November 2, 2013

Revised: January 28, 2014

Accepted: February 19, 2014

Published: February 19, 2014

Scheme 1. Sketch for the Preparation of TiO₂/CdS Nanocomposites

Surfactants. Capped-TiO₂ nanorods were synthesized at low temperatures using the solvothermal method. Oleic acid (OA), and 6-aminohexanoic acid (6AHA) were used as surfactants with various molar ratios. A mixture of 1 mmol TB, 6AHA, OA, and absolute ethanol (EtOH) with desired precursor molar ratios was mixed well and stirred for 30 min under room temperature before being transferred into a Teflon-lined stainless steel autoclave. The autoclave also contained about 5–10 mL of EtOH in order to keep equilibrium in the mixture and to avoid any change in EtOH concentration during the crystallization process. The synthesis process was set at 140 °C for 18 h. After that, the autoclave was cooled down slowly to room temperature, and samples were collected and washed several times using ethanol and toluene.

2.3. Development of TiO₂ Nanorods by Ligand Exchange Reaction. Typically, 5 mL of dichloromethane solution of NOBF₄ (0.01M) was added to hexane solvent containing capped-TiO₂ nanorods at room temperature. The mixture was then gently shaken until the precipitation of the TiO₂ nanorods. These nanorods quickly become insoluble and are collected through centrifugation. Then, they were redispersed in DMF hydrophilic solvent. To purify the TiO₂ nanorods, DMF solutions were washed through the addition of a mixture of toluene and ethanol 95% until precipitation occurs then followed by centrifugation. This process was repeated few times. Finally, the collected TiO₂ nanorods were dried overnight in oven at 65 °C to remove residual solvent molecules.

2.4. Synthesis of Colloidal Hybrid TiO₂/CdS Nanocomposite. A mixture of 4.5 mmol of NOBF₄-capped-TiO₂ nanorods dispersed in 10 mL of DMF, and 9 mmol cadmium acetate dihydrate was stirred under room temperature for 2 h. Subsequently, 9 mmol thioamide was added to the mixture and let under stirring for an additional 3 h in order to ensure a complete reaction. The precipitated TiO₂/CdS nanocrystals were washed few times using toluene and ethanol 95%, and then collected by centrifugation.

2.5. Synthesis of Ni–TiO₂/CdS by a Photodeposition Method. Typically, Ni(NO₃)₂ was added to the solution containing TiO₂/CdS. Because the surface of TiO₂ is negative, positive charge Ni²⁺ is selectively absorbed on the TiO₂ surface, leading to the formation of TiO₂/CdS–Ni²⁺. This solution is then illuminated with visible light for 1.5 h. As the potential of Ni²⁺/Ni is lower than the conduction band level of TiO₂, the electrons from the latter can effectively reduce Ni²⁺ species adsorbed on their surface, forming a metallic Ni cluster.¹⁸

2.6. Characterization. Transmission Electron Microscopy (TEM) Images of TiO₂ nanorods, and hybrid TiO₂/CdS NCs

were obtained on a JEOL JEM 1230 operated at 120 kV. Samples were prepared as follows: a drop of a dilute toluene dispersion of nanocrystals were deposited onto a 200 mesh carbon-coated copper grid then evaporated immediately at ambient temperature. Elemental dispersive spectrum (SEM-EDX) analysis was obtained from a JEOL 6360 instrument working at 3 kV. Powder X-ray diffraction (XRD) patterns of the samples were obtained on a Bruker SMART APEXII X-ray diffractometer equipped with a Cu K α radiation source ($\lambda = 1.5418 \text{ \AA}$) in the 2θ range of 5–20° at a scan rate of 1.0°/min. All samples were dried at 65 °C overnight to eliminate guest solvent molecules on the surface of particles before the XRD scan. Fourier transform infrared absorption spectra (FTIR) were measured with a FTS 45 infrared spectrophotometer in the spectral range of 4000–400 cm⁻¹. The thermal analyses of the as-made TiO₂ nanorods, CdS NPs, and hybrid TiO₂/CdS NCs were carried out at a heating rate of 10 °C/min up to 900 °C under an oxygen flow using a Perkin-Elmer TGA thermogravimetric analyzer. The UV–visible spectra of the nanostructures were recorded for the powder sample on a Cary 300 Bio UV–visible spectrophotometer, and pure magnesium oxide (MgO) was used as a blank. ζ -Potential measurements were performed with a Zetasizer Nano ZS in water at 25 °C. Nitrogen adsorption/desorption isotherms of the samples were obtained using with a Quantachrome Autosorb-1 system, after degassing at 100 °C and 10–5 mmHg for at least 5 h. The specific surface areas (SBET) of the samples were calculated from adsorption isotherm data using the standard Brunauer–Emmett–Teller (BET) method. XPS characterization was carried out in order to analyze the chemical composition of composite, as well as the electronic state of Ni in the sample. XPS measurement was done in an evacuated ion-pumped chamber at 1×10^{-9} Torr of Kratos Axis-Ultra instrument. The X-ray source is a monochromatic Al source (Al K α , $h\nu = 1486.6 \text{ eV}$) operated at 300 W. The binding energy of samples was measured by fixing an internal reference C1s peak at 285.0 eV. For the separate constituents after background subtraction, all the peaks were deconvoluted by means of standard CasaXPS software.

2.7. Photocatalysis Characterization (Photocatalytic H₂ Evolution). Before photocatalytic characterization, the surfactants adsorbed on samples were eliminated. These samples were dried overnight at 65 °C and used as such for photocatalytic measurement. Visible-light-induced H₂ evolution was carried out in 80 mL septum-sealed glass vials. A mixture of 20 mg of sample and 3% Ni²⁺ were dispersed well in 27 mL of aqueous solution containing ethanol (25 wt%). The vial was deoxygenated using nitrogen and then placed in front of 300 W

Xe lamp with a 420 nm cutoff filter (FSQ-GG420) for catalytic reaction. Gaseous products were then identified by collecting 0.5 mL of the gas in the headspace of the vials. This gas was then analyzed by gas chromatography (GC) using a thermal conductivity detector (TCD) for the quantification of H_2 with Ni as the carrier.

3. RESULTS AND DISCUSSIONS

Scheme 1 shows the procedure adopted for the synthesis of surfactant capped- TiO_2 nanorods by the hydrolysis of a titania precursor followed by a solvothermal reaction in autoclave. First, an ethanol solution of titanium(IV) butoxide (TB) was modified by hydrolysis with OA and 6AHA as surfactants. The hydrolysis process helped to yield three-dimensional polymeric titania skeletons, which acted as the seeds for titania growth. To obtain the desired TiO_2 uniform sizes of particles, the subsequent solvothermal process was carefully controlled with presetting the reaction time (18 h) and temperature (140 °C). It was observed that TiO_2 nanorods were always achieved with the use of OA and 6AHA as surfactants.

3.1. TEM, FTIR, AND BET CHARACTERIZATION

Figure 1 shows TEM image of the obtained TiO_2 nanorods before sonication. As seen in the TEM image, these nanorods

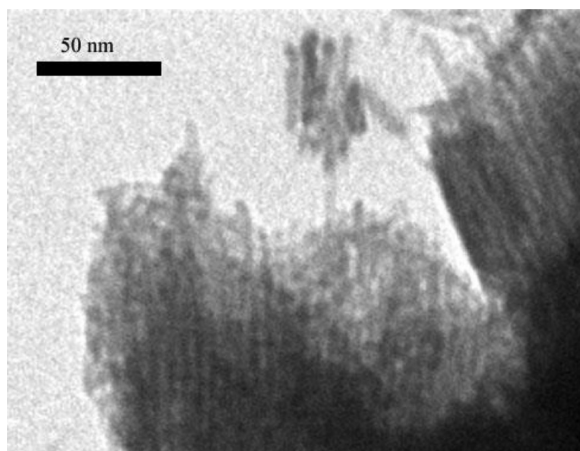


Figure 1. TEM image of the synthesized TiO_2 nanorods before sonication.

were attached together in a parallel configuration to form big aggregation. This is different from the results obtained by Dinh et al.¹⁹ who showed well-dispersed TiO_2 nanorods by using OA and oleylamine as surfactants. The aggregation obtained in our approach may be due to the replacement of oleylamine by the 6AHA surfactant.

Figure 2 also shows TEM images of TiO_2 nanorod samples obtained with different molar TB:OA:6AHA ratios after a few minutes of sonication. As seen in Figure 2, by varying the molar ratio between TB, OA, and 6AHA, different sizes of TiO_2 nanorods were observed. For a TB:OA:6AHA molar ratio of 1:7:3, TiO_2 nanorods of 3×40 nm were achieved (Figure 2a). When the concentration of 6AHA was increased from 3 to 10 (e.g., from 1:7:3 to 1:7:10), while the TB and OA concentrations kept the same, the shape of TiO_2 nanorods did not change; however, the length of the nanorod was decreased from 40 to 10 nm (Figure 2b). Hence, it could be assumed that the length of TiO_2 nanorods is controlled by the molar ratio OA:6AHA. Also, it should be mentioned that OA

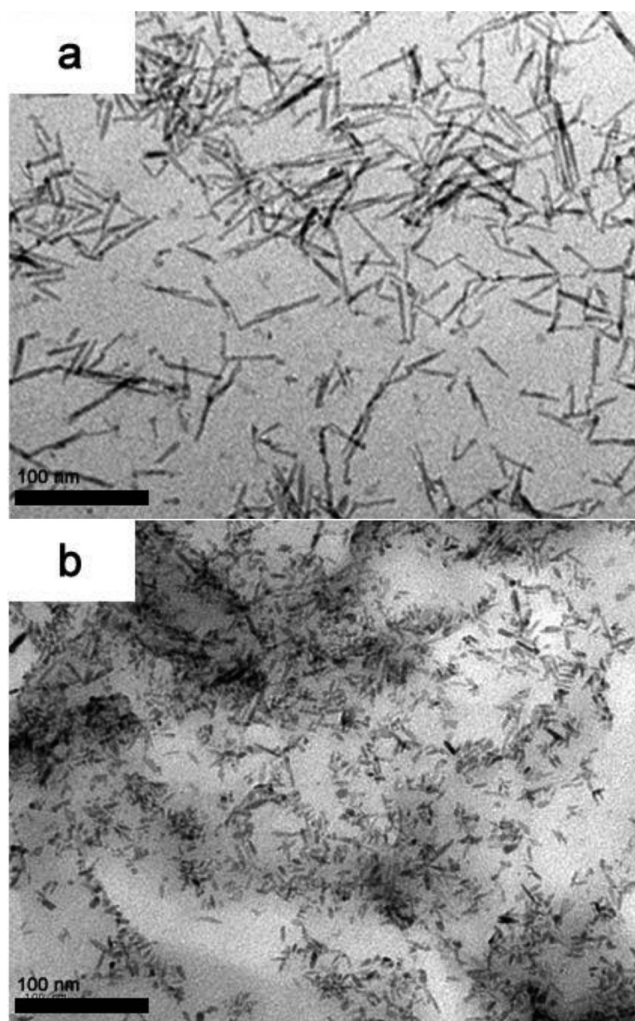


Figure 2. TEM images of synthesized TiO_2 nanorods after sonication: (a) 3×40 nm nanorods for TB:OA:6AHA molar concentration of 1:7:3 and (b) 3×10 nm nanorods for TB:OA:6AHA molar concentration of 1:7:10.

and 6AHA surfactants have selective bindings to the different faces of TiO_2 . Joo et al.²⁰ reported that OA binds strongly to the TiO_2 {001} faces, while 6AHA binding is more favored on {101} faces. When the concentration of 6AHA is high (OA:6AHA molar ratio = 7:10), the strong adhesion of 6AHA to the low surface energy {101} face, compared to the adhesion of OA to {001} face, leads to a less progressive TiO_2 growth along {001} direction to form TiO_2 nanorods with short length. By decreasing the molar concentration of 6AHA, the adhesion of 6AHA to the low surface energy {101} decreases while the adhesion of OA to {001} is kept the same. The growth along {001} is then preserved, leading to longer TiO_2 nanorod shape.²¹

Because OA and 6AHA were used as capping agents, the hydrophobic surfactant capped- TiO_2 nanorods were soluble in nonpolar hydrophobic solvents, such as toluene and hexane. However, after being treated with dichloromethane solution of $NOBF_4$, TiO_2 nanorods precipitated immediately in hexane solvent after gentle shaking indicating that $NOBF_4$ has replaced the original hydrophobic surfactant capped to the nanorod surface. This also indicates a dramatic change in surface properties of these NPs, from hydrophobic to hydrophilic. As seen in Figure 3, it was observed that $NOBF_4$ capped- TiO_2

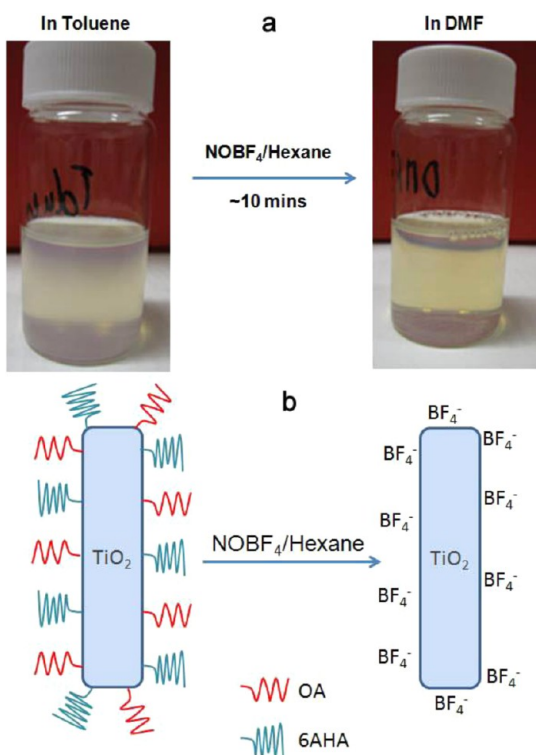


Figure 3. (a) Surfactant-capped TiO₂ nanorods dissolved in toluene; (b) TiO₂ nanorods after NOBF₄ treatment dissolved in DMF.

nanorods were easily redissolved in DMF solvent as well as in water. This is considered as an advantage during the deposit process of CdS on the surface of TiO₂ nanorods since both cadmium acetate and thioamide are well dissolved in DMF. A higher dispersion of the initial precursors in the media (TiO₂, Cd²⁺, S²⁻) increases the chance to achieve uniform TiO₂ nanorods with a higher dispersion of CdS on their surface.

To analyze the surface properties of TiO₂ nanorods, FTIR characterization was done for the samples before and after surfactant treatment. The corresponding results are shown in Figure 4. FTIR spectra of the capped TiO₂ nanorods before surface treatment with NOBF₄ and those of OA and 6AHA surfactants are shown in Figure 4a. The small peaks at 3004 cm⁻¹ were observed in the both FTIR spectra of OA and 6AHA, corresponding to the stretching of =C—H bond. The sharp vibrations bands at 2916 and 2857 cm⁻¹ are attributed to the asymmetric and symmetric C—H bonds in methylene groups (CH₂),²² respectively. The peaks at 1714 and 1282 cm⁻¹ in the spectrum of OA are assigned to C=O and C—O stretching and those appearing at 1463 and 936 cm⁻¹ are due to in-plane and out-of-plane O—H. Compared to the commercial P25—TiO₂, our synthesized TiO₂ nanorods are identified by the additional peaks at 3004, 2922, 2853, and 1465 cm⁻¹ due to the presence of capping ligand on the surface. In addition, the peak appearing at 1608 cm⁻¹ indicates the existence of carboxylic acid salt on the surface of surfactant capped-TiO₂ nanorods, which is the result of the reaction between the OA surfactant and TiO₂ during the solvothermal process. Furthermore, a weak peak at 1041 cm⁻¹ in the sample of surfactant capped-TiO₂ nanorods, which corresponds to that of C—N bonds in the amine groups, proves the existence of amine on their surface (resulting from the 6AHA surfactant).

Figure 4b shows the FTIR spectrum of the TiO₂/CdS NCs after surface treatment. No essential peak characteristic of —C—

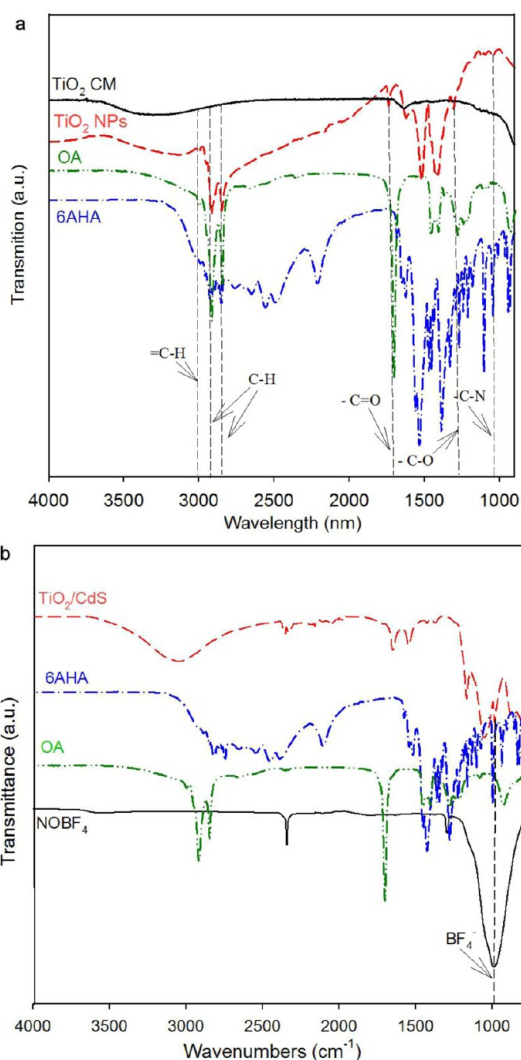


Figure 4. FTIR of (a) capped-TiO₂ nanorod synthesized using OA and 6AHA as surfactants; (b) TiO₂/CdS nanoparticles.

H stretching vibration at 2800–3000 cm⁻¹ was observed after CdS deposition, as compared to that of the sample before deposition. This could be due to NOBF₄ treatment process where CdS deposition was able to remove some residues of OA and 6AHA molecules attached to TiO₂ nanorods surface (see Figure 4). As will be presented later (TGA characterization), this could explain the difference of weight loss between TiO₂ nanorods and TiO₂/CdS nanocomposite. Furthermore, in comparison with the FTIR spectrum of TiO₂ nanorods before NOBF₄ treatment, there is a small peak at around 1000 cm⁻¹, which is assigned to BF₄⁻ anions. Furthermore, no peak is observed around 2100–2200 cm⁻¹, which is normally ascribed to NO⁺. This is an indication that surfactant exchange was between the organic ligands and inorganic BF₄⁻, not with NO⁺. The big peak at around 3050 cm⁻¹ on the FTIR spectrum of TiO₂/CdS, which is similar to the peak observed for commercial TiO₂ nanorods, is attributed to the water absorbed on the surface of TiO₂/CdS nanocomposite.

Figure 5 shows TEM image and Brunauer–Emmett–Teller (BET) adsorption/desorption isotherm curves for the sample of TiO₂/CdS nanocomposites. As seen in Figure 5a, TiO₂/CdS nanoparticles were aggregated to form hollow nanospheres with a uniform diameter of around 150 nm. When water sonication

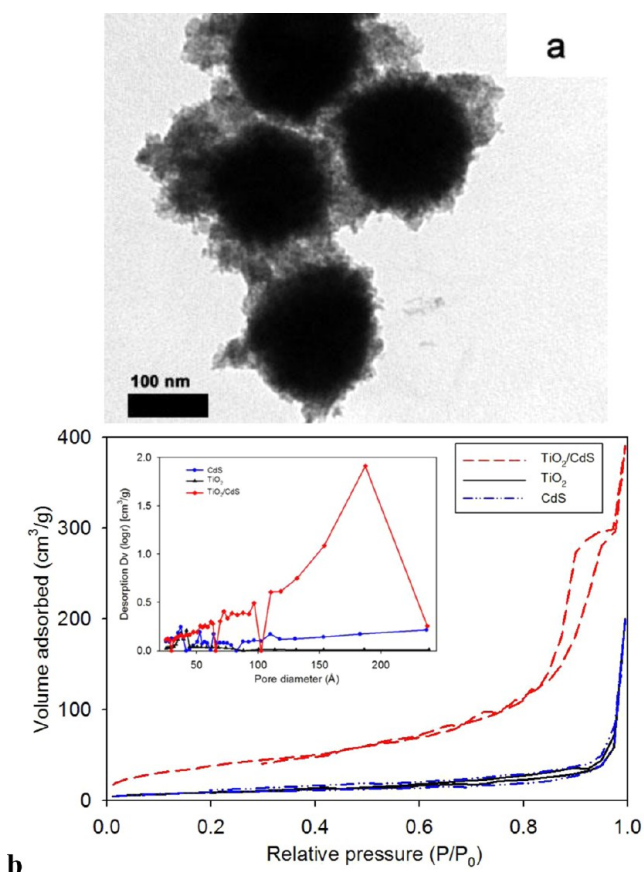


Figure 5. (a) TEM image of TiO_2/CdS nanocomposite and (b) BET characterization of TiO_2 , CdS, and TiO_2/CdS nanocomposite with the inset is their corresponding pore size distribution.

was performed, hollow nanospheres were separated from each other. However, single nanospheres were not separated into single NPs by sonication at low frequency ultrasound. Because the TiO_2/CdS hollow nanospheres are composed of a large number of nanoparticles, a high surface area can be expected, as shown in Figure 5b. The BET specific surface area is $146 \text{ m}^2/\text{g}$, which is much higher than that of TiO_2 nanorod ($27.5 \text{ m}^2/\text{g}$) and of CdS cubic ($34.7 \text{ m}^2/\text{g}$). The surface area results are in agreement with the observation from the isotherm figure, which shows that the isotherms of TiO_2/CdS shift up compared to those of TiO_2 and CdS.

The pore size distribution curves (see inset, Figure 5b) calculated from the desorption branch of the nitrogen isotherms by the BJH method show a wide range of pore diameters (from 5 to 237 nm) with a peak at a pore diameter of about 166 nm. Meanwhile, a distinct hysteresis loop can be observed between adsorption and desorption branches, in the range of 0.8 to 1 nm, which is an indication of mesostructured the TiO_2/CdS nanospheres.^{23,24}

3.2. XRD Characterization. Figure 6 shows XRD patterns of TiO_2 nanorods, CdS NPs, and TiO_2/CdS nanocomposites. XRD patterns of TiO_2 nanorods exhibit strong diffraction peaks at 25° and 48° , indicating a TiO_2 anatase phase. All peaks were in good agreement with the standard spectrum for TiO_2 (JCPDS nos 88-1175 and 84-1286). Meanwhile, it is known that CdS NPs possess the hexagonal phase with (002) as the preferential crystalline plane with two main peaks at 28.3° (101 planes) and 48.1° (103 planes),²⁵ while the cubic phase has three main peaks at 26.5° (111 planes), 43.9° (220 planes), and

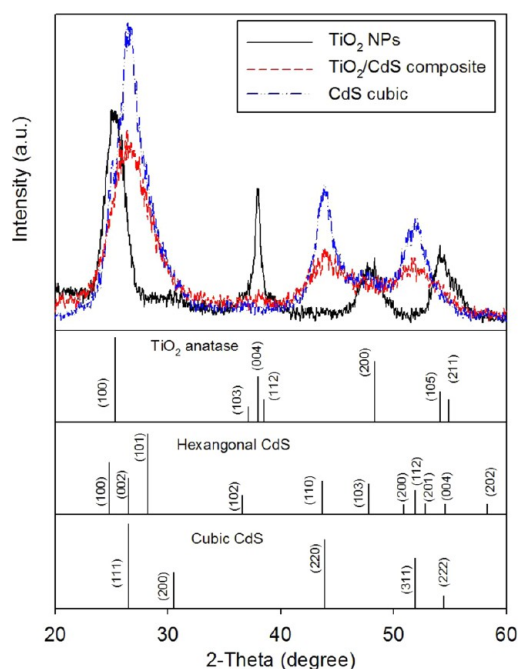


Figure 6. XRD characterization of (a) TiO_2 nanorod and (b) TiO_2/CdS nanocomposite.

51.9° (311 planes).¹³ Hence, with those peaks shown in the XRD pattern of CdS NPs, we can conclude that CdS NPs are in cubic phase.

XRD patterns of the TiO_2/CdS nanocomposites confirm the presence of CdS and TiO_2 . However, when mixed with high concentration of CdS NPs, the intensity of the diffraction peaks at 48° was very low, which could be due to the attachment of CdS on the surface of TiO_2 nanorods. In the XRD spectrum of our TiO_2/CdS nanocomposite, three broad and symmetric peaks were observed at $2\theta = 26.5^\circ$ (111 planes), 43.9° (220 planes), and 51.9° (311 planes), corresponding to the cubic phase of CdS. The absence of planes referring to hexagonal structured CdS indicates the presence of only cubic CdS nanoparticles in the sample. Furthermore, the broadening of the peaks is due to the CdS nanosize in the TiO_2/CdS nanocomposite.

3.3. XPS and SEM-EDX Characterization. The XPS survey spectrum (Figure 7a) shows the existence of Ti, O, Cd, S, Ni, and C elements in the sample. Also, the high-resolution XPS spectrum of Ni 2p_{3/2} peak at 856.4 eV confirms the presence of Ni in the sample (Figure 7b), mainly from NiO.^{26,27} The formation of NiO could be due to the photoinduced electrons in the conduction band of TiO_2 transferred to Ni^{2+} clusters causing the reduction of a part of Ni^{2+} clusters to NiO atoms due to their instability in the air.²⁷ In addition, the Ti2p and O1s peaks are respectively found at 458.6 and 530.95 eV, which are compatible with the assignment to TiO_2 . Cd3d (405.1 eV) and S2p (161.95 eV) peaks are reported to be compatible with CdS. The observation of C1s element is due to the surfactant capped on the surface of the sample, and also from the adventitious hydrocarbon in the XPS instrument itself. The XPS peak at 686.91 eV is ascribed to F^- ions coming from NOBF_4 during surfactant treatment process.

The presence of Ni in the sample was also confirmed from the SEM-EDX elemental analytical spectrum (Figure 8). This spectrum shows that the intensity of Ni peak is small compared to the other elements. This is due to the small amount of Ni

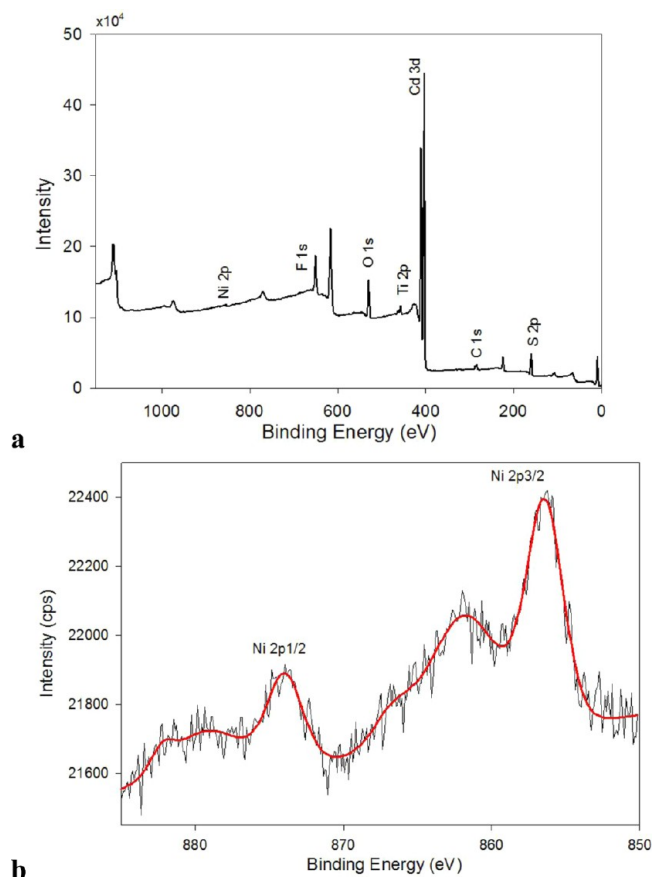


Figure 7. (a) XPS characterization of Ni-TiO₂/CdS nanocomposite and (b) high-resolution XPS of Ni.

cluster deposited on the TiO₂/CdS composite, which is only 3 wt%.

3.4. UV/Vis and Photoluminescence (PL) Characterizations. The optical properties of TiO₂ nanorods before

surface treatment and TiO₂/CdS nanocomposites were investigated by UV/vis absorption and photoluminescence (PL) characterization techniques. The UV-visible absorption spectrum (Figure 9a) has been performed to measure the photoresponse of TiO₂ nanorods after their loading with CdS. The absorption edge for anatase TiO₂ nanorod is approximately 380 nm (3.12 eV), which has no significant absorption in visible-light region. However, the spectrum of CdS exhibits a broad absorption band around 530 nm (2.32 eV), indicating the effective photoabsorption property in the visible region. Basically, the spectrum of TiO₂/CdS nanocomposite is a combination of TiO₂ and CdS spectra. The absorption edges of the TiO₂/CdS nanocomposite are at approximately 547 nm (2.23 eV), which is around 15 nm red-shift than that of CdS. This probably results from the coupling between CdS and TiO₂.

Figure 9b shows the PL emission spectra for CdS and TiO₂/CdS nanocomposites at room temperature under light excitation at a wavelength of 380 nm. According to the PL of both CdS and TiO₂/CdS sample, PL peak of TiO₂/CdS exhibited much weaker intensity than of that of CdS. The decrease in PL intensity indicates a better PL quenching, which also indicates a decrease in light emission of the material or a coupling between CdS and TiO₂ with a better charge transfer between these two nanoparticles. As discussed above, the efficient charge transfer from CdS to TiO₂ conduction band could effectively separate the photoinduced electrons from holes in the CdS semiconductor. Thus, the decrease in PL intensity also could be ascribed to the lower recombination probability of photoinduced electrons and holes in the TiO₂/CdS nanocomposite.²⁸

3.5. Thermal Gravimetric (TGA) and ζ-Potential Characterization. Thermal gravimetric characterization of synthesized capped TiO₂ nanorods, CdS NPs, and TiO₂/CdS nanocomposites are summarized in TGA curves of Figure 10, which were obtained at a heating rate of 10 °C/min under O₂ atmosphere. All the three curves show an initial weight loss

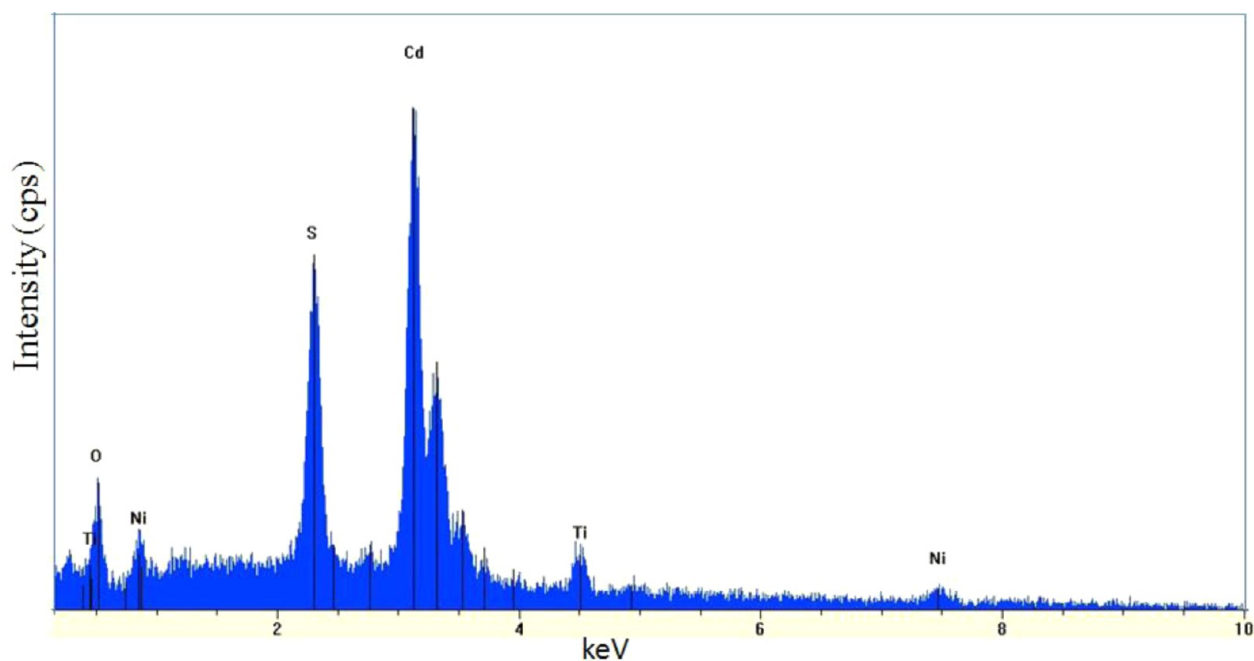


Figure 8. SEM-EDX characterization of Ni-TiO₂/CdS nanocomposite.

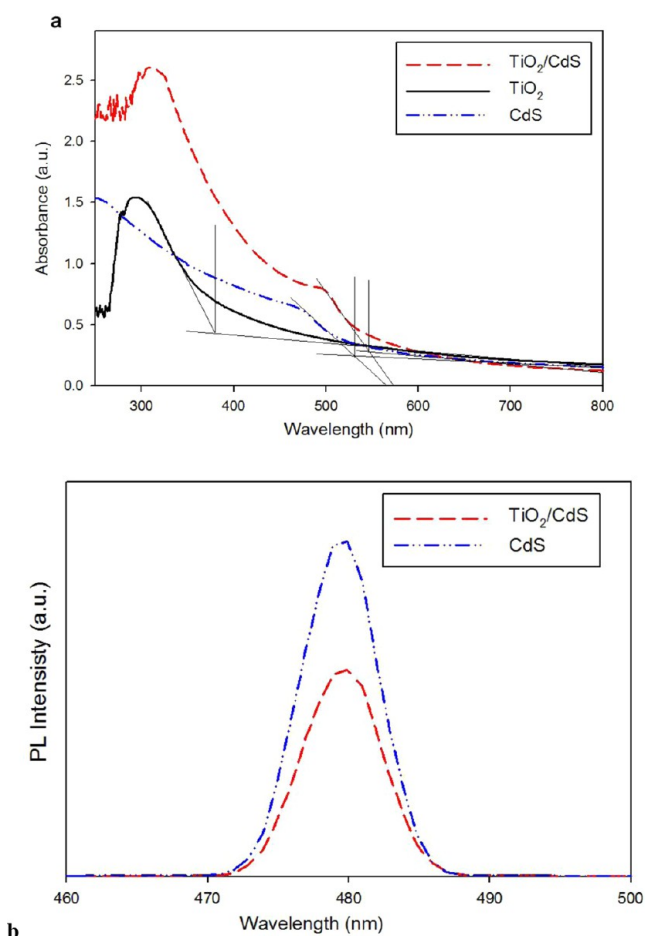


Figure 9. (a) UV-vis spectra of TiO₂, CdS, and TiO₂/CdS. (b) Photoluminescence (PL) emission spectra under excitation at a wavelength of 380 nm for CdS and TiO₂/CdS nanocomposite.

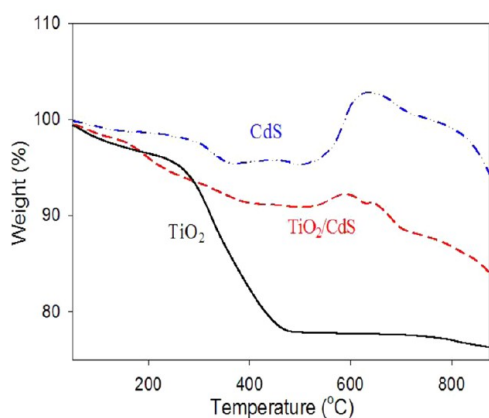


Figure 10. TGA characterization of (black) TiO₂ nanorods, (blue) CdS NPs, and (red) TiO₂/CdS nanocomposites.

starting at around 50 °C, which could be attributed to the water absorbed on the surface of the nanoparticles. For TiO₂ nanorods, the most significant weight loss obviously occurred between 200 and 480 °C and corresponds to OA surfactants. For higher temperatures (>480 °C), the very small weight loss could be attributed to the decomposition of residual product traces that forms a sheath over the TiO₂ nanorods. For CdS NPs, the TGA spectrum shows that the main mass decrease occurred below 400 °C, which could be mainly due to the

evaporation of residual solvent. A non-negligible gain in mass was also observed between 400 and 750 °C, which is an indication of the formation of cadmium sulfate (CdSO₄) through the following reaction (eq 1).²⁹ The decomposition of CdSO₄ starts at 750 °C leading to a further decrease in mass.



The TGA behavior of the TiO₂/CdS nanocomposite is basically a combination of TiO₂ and CdS behaviors. The weight loss below 200 °C could be attributed to the water absorbed on the surface of particles, while weight loss from 200 to 400 °C could be due to the loss of the rest of surfactant on the surface of TiO₂. The mass increase observed at the same temperature level corresponding to the increase in CdS mass, is due, as mentioned above, to the formation of the intermediate product, CdSO₄.

The ζ -potential curves of TiO₂ nanorods before and after NOBF₄ treatment, CdS NPs, and TiO₂/CdS nanocomposites are shown in Figure 11. According to these curves, the charge

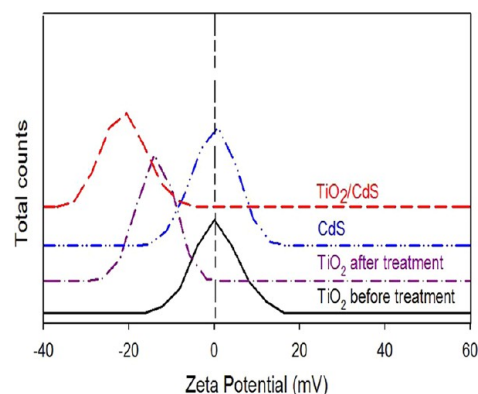


Figure 11. ζ -Potential distributions in aqueous solution at pH ~ 5 of TiO₂ nanorods before and after treatment with NOBF₄ surfactant, CdS NPs, and TiO₂/CdS nanocomposite.

surface potential of TiO₂ nanorods before surfactant exchange was zero at pH = 5. However, when treated with NOBF₄, the surface of TiO₂ nanorods was negatively charged, which is in agreement with the results reported by Dong et al.³⁰ Because the surface of TiO₂/CdS is negatively charged, Ni clusters were selectively deposited (by using photodeposition technique) as cocatalysts on the surface of TiO₂/CdS composite. In this case, Ni²⁺ is selectively adsorbed on the surface of TiO₂ nanorods, not on the surface of CdS (because the ζ -potential of CdS is zero), due to the electrokinetic potential preferable in colloidal systems. Under visible-light illumination, the generated electrons from the conduction band of CdS are transferred to the conduction band of TiO₂. Because the conduction band level of Ni²⁺/Ni is lower than that of TiO₂, the electrons from the conduction band of TiO₂ are able to reduce Ni²⁺ to form metallic Ni clusters on the surface of TiO₂ nanorods (Scheme 1).

3.6. Photocatalytic Activity. The photocatalytic activity of TiO₂, CdS, and TiO₂/CdS nanocomposite with Ni cocatalyst for H₂ generation were carried out under visible-light irradiation ($\lambda > 420$ nm) using ethanol as a sacrificial reagent. As seen from Figure 12a, TiO₂ nanorods are not able to generate H₂ because TiO₂ nanorods do not absorb visible light and consequently could not generate electron-hole to support the H₂ evolution. Besides, CdS alone shows very low H₂

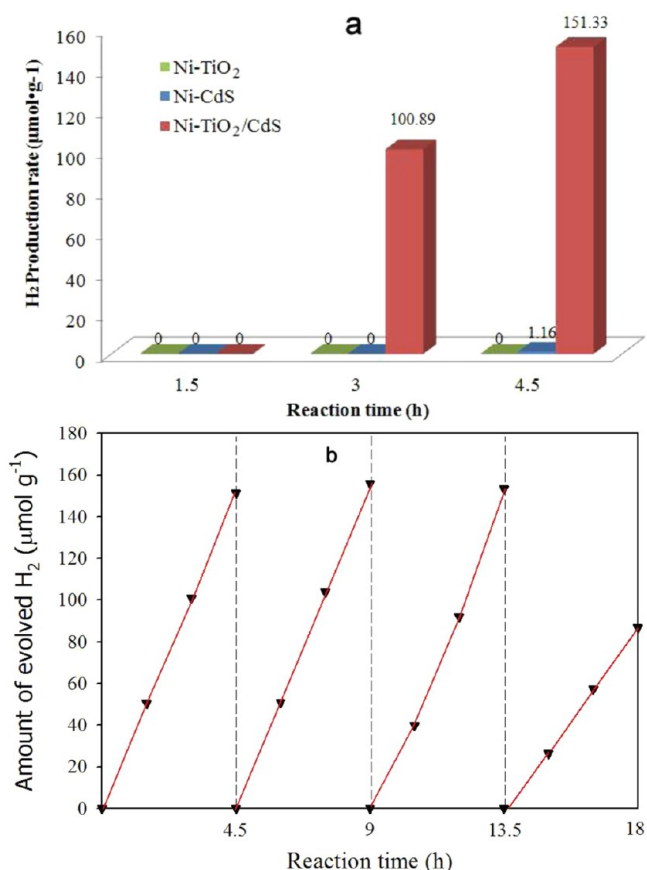


Figure 12. (a) Comparison of the activity of H₂ evolution using different photocatalysts; (b) H₂ production from TiO₂/CdS-Ni photocatalyst monitored over 18 h. Each 4.5 h, the reaction system is bubbled with N₂ to remove the H₂ inside.

generation rates, only $0.77 \mu\text{mol}\cdot\text{h}^{-1}\cdot\text{g}^{-1}$ after 4.5 h of reaction. The low rate could be due to the rapid recombination of photogenerated electrons and holes, which resulted in the lack of H₂ evolution sites.^{31,32} The coupling of CdS with TiO₂ nanorods shows a big improvement in H₂ production; around $33.63 \mu\text{mol}\cdot\text{h}^{-1}\cdot\text{g}^{-1}$ of H₂ was evolved, which is around 44

times higher than the production for the Ni-CdS system. The rate of Ni-TiO₂/CdS photocatalytic activity is also reported to be faster compared to that of Ni-CdS, which could be due to a better charge transfer between CdS and TiO₂, as shown and discussed above (Figure 9). The photocatalytic performance of TiO₂/CdS without a Ni cocatalyst using ethanol as a sacrificial reagent was also carried out; however, the H₂ production evolution maybe was too low, and so we would not be able to detect the signal of activity. In other words, without using Ni as a cocatalyst, the composite TiO₂/CdS is not active for photocatalytic H₂ production using visible light.

To investigate the stability of Ni-TiO₂/CdS samples, a series of tests composed of four cycles with intermittent deoxygenation were carried out without catalyst regeneration. Between each cycle, the reaction system was bubbled with N₂ to remove H₂. As shown in Figure 12b, the results show good stability for the photocatalyst up to 15 h of irradiation without noticeable catalytic deactivity; however, after 15 h of reaction, the activity is decreased by about 50%. Even though the photocatalyst was decreased after 15 h of irradiation, this achievement is still considered as a good improvement for the photocatalytic activity of metal sulfides, which are often unstable for conventional CdS photocatalysts, due to the reduction of metal cations in metal sulfides by generated electrons, and the oxidation of S²⁻ by generated holes.³¹⁻³³

In Ni-TiO₂/CdS nanocomposite, with the support of TiO₂ nanorods, the photo-oxidation is avoided due to the electrons transfer from the conduction band of CdS to that of TiO₂ and then to the metallic cocatalyst (Ni), therefore it would prevent Cd²⁺ from reduction. In addition, under visible-light illumination, only CdS with a small bandgap energy of 2.4 eV can generate holes in the valence band (VB). However, because the VB of CdS (+1.5 V vs SHE) is smaller than the VB of TiO₂ (+3.4 V vs SHE),^{34,35} these holes in the VB of CdS cannot be transferred to the VB of TiO₂. Thus, Ni clusters, which are only located on the surface of TiO₂, are cannot be oxidized by holes in the VB of CdS NPs. Therefore, with those mentioned special features above, it is not surprising to see that Ni-TiO₂/CdS nanocomposite exhibits not only high activity but also good stability in the photocatalyst production of H₂ up to 15 h of irradiation.

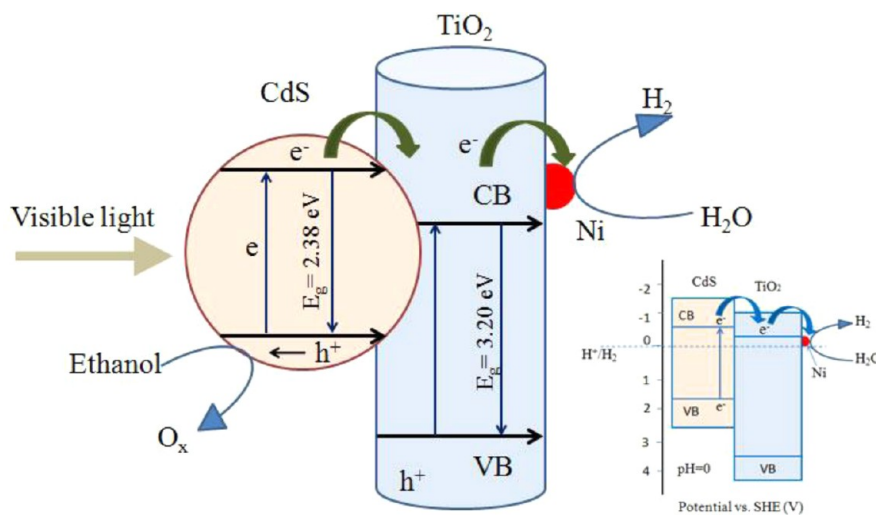
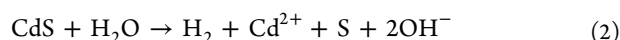


Figure 13. Mechanism illustration of the activity of Ni-TiO₂/CdS under visible light for the production of H₂; inset is the potential redox energy corresponding to CdS, TiO₂, and H⁺/H₂.

The mechanism of H₂ production activity of Ni–TiO₂/CdS under visible light is illustrated in Figure 13. The full mechanism could be similar to the mechanism of Pt–TiO₂/CdS, which was reported in literature.³⁶ When the coupled TiO₂ and CdS semiconductors are activated under the visible light, electrons and holes are generated in the conduction and valence bands of CdS. Furthermore, due to the different bandgap positions, the generated electrons from the conduction band of CdS are transferred toward TiO₂ conduction band. As the Ni clusters are preferentially attached on TiO₂ nanorod instead of CdS NPs, they would be able to cap the electron from the conduction band of TiO₂, and act as H₂ evolution.

Meanwhile, the holes at the valence band of CdS are responsible for oxidizing ethanol and may also anodically autocorrode the CdS particles.^{37,38} If the photogenerated holes do not react quickly with Cd–OH groups or ethanol, the photocorrosion of CdS occurs and induces a release of ion cadmium in solution leading to the formation of cadmium hydroxide layer on the surface of the CdS particles, as shown by the following equation:



Also, if the surface of CdS NPs is covered with cadmium hydroxide, this causes sulfide vacancies saturation; hence the holes can no longer being trapped. The recombination of generated electrons and holes will then be faster.³⁹ With those two reasons, it would be expected to see a decrease in the photocatalysis activity of the Ni–TiO₂/CdS system after 15 h of reaction.

3. CONCLUSION

In conclusion, we developed a new hybrid photocatalytic system for the production of H₂ under visible-light illumination using ethanol as a sacrificial agent, which was based on a TiO₂ nanorods, CdS nanoparticles, and a Ni cluster cocatalyst. In a first time and due to the fact that OA and 6AHA surfactants have selective bindings to the different faces of TiO₂, different sizes of TiO₂ nanorods were obtained varying the molar ratio between TB, OA, and 6AHA. A three-step synthesis process was then used to develop the TiO₂/CdS–Ni nanocomposite photocatalyst. Under visible-light illumination and due to the fact that electron–hole separation was highly enhanced, the developed TiO₂/CdS–Ni photocatalyst showed a high photocatalytic performance for the H₂ production, which was around 44 times higher than that of Ni–CdS. In addition, this hybrid composite photocatalyst appeared to exhibit a high photocatalytic performance for the production of hydrogen (H₂).

AUTHOR INFORMATION

Corresponding Author

*F. Mighri. E-mail: Frej.Mighri@gch.ulaval.ca. Tel.: (418) 656-2241. Fax: (418) 656-5993.

Notes

The authors declare no competing financial interest.

ACKNOWLEDGMENTS

The authors thank the Natural Sciences and Engineering Research Council of Canada (NSERC) for financial support of this work.

REFERENCES

- (1) Liao, C.-H.; Huang, C.-W.; Wu, J. C. S. Hydrogen Production from Semiconductor-based Photocatalysis via Water Splitting. *Catalysts* **2012**, *2*, 490–516.
- (2) Wang, D.; Li, D.; Guo, L.; Fu, F.; Zhang, Z.; Wei, Q. Template-Free Hydrothermal Synthesis of Novel Three-Dimensional Dendritic CdS Nanoarchitectures. *J. Phys. Chem. C* **2009**, *113*, 5984–5990.
- (3) Rao, B. S.; Kumar, B. R.; Reddy, V. R.; Rao, T. S. Preparation and characterization of CdS nanoparticles by chemical co-precipitation technique. *Chalcogenide Lett.* **2011**, *8*, 177–185.
- (4) Matsumura, M.; Furukawa, S.; Saho, Y.; Tsubomura, H. Cadmium sulfide photocatalyzed hydrogen production from aqueous solutions of sulfite: effect of crystal structure and preparation method of the catalyst. *J. Phys. Chem.* **1985**, *89*, 1327–1329.
- (5) Chen, X.; Shangguan, W. Hydrogen production from water splitting on CdS-based photocatalysts using solar light. *Front. Energy* **2013**, *7*, 111–118.
- (6) Rajendran, V.; Lehnig, M.; Niemeyer, C. M. Photocatalytic activity of colloidal CdS nanoparticles with different capping ligands. *J. Mater. Chem.* **2009**, *19*, 6348.
- (7) Daghri, R.; Drogui, P.; Robert, D. Modified TiO₂ For Environmental Photocatalytic Applications: A Review. *Ind. Eng. Chem. Res.* **2013**, 3581–3599.
- (8) Xiang, Q.; Yu, J.; Jaroniec, M. Synergetic effect of MoS₂ and graphene as cocatalysts for enhanced photocatalytic H₂ production activity of TiO₂ nanoparticles. *J. Am. Chem. Soc.* **2012**, *134*, 6575–8.
- (9) Wang, X.; Liu, G.; Chen, Z.-G.; Li, F.; Wang, L.; Lu, G. Q.; Cheng, H.-M. Enhanced photocatalytic hydrogen evolution by prolonging the lifetime of carriers in ZnO/CdS heterostructures. *Chem. Commun.* **2009**, 3452–4.
- (10) Li, X.-H.; Zhang, J.; Chen, X.; Fischer, A.; Thomas, A.; Antonietti, M.; Wang, X. Condensed Graphitic Carbon Nitride Nanorods by Nanoconfinement: Promotion of Crystallinity on Photocatalytic Conversion. *Chem. Mater.* **2011**, *23*, 4344–4348.
- (11) Xiang, Q.; Yu, J. Graphene-Based Photocatalysts for Hydrogen Generation. *J. Phys. Chem. Lett.* **2013**, *4*, 753–759.
- (12) Chen, X.; Mao, S. S. Titanium dioxide nanomaterials: synthesis, properties, modifications, and applications. *Chem. Rev.* **2007**, *107*, 2891–959.
- (13) Li, G.-S.; Zhang, D.-Q.; Yu, J. C. A New Visible-Light Photocatalyst: CdS Quantum Dots Embedded Mesoporous TiO₂. *Environ. Sci. Technol.* **2009**, *43*, 7079–7085.
- (14) Stengl, V.; Kralova, D. TiO₂/ZnS/CdS Nanocomposite for Hydrogen Evolution and Orange II Dye Degradation. *Int. J. Photoenergy* **2011**, *2011*, 1–14.
- (15) Bai, S.; Li, H.; Guan, Y.; Jiang, S. The enhanced photocatalytic activity of CdS/TiO₂ nanocomposites by controlling CdS dispersion on TiO₂ nanotubes. *Appl. Surf. Sci.* **2011**, *257*, 6406–6409.
- (16) Shangguan, W. Hydrogen evolution from water splitting on nanocomposite photocatalysts. *Sci. Technol. Adv. Mater.* **2007**, *8*, 76–81.
- (17) Gopidas, K. R.; Bohorquez, M.; Kamat, P. V. Photophysical and Photochemical Aspects of Coupled Semiconductors. Charge-Transfer Processes In Colloidal CdS–TiO₂, and CdS–AgI Systemst. *J. Phys. Chem.* **1990**, *94*, 6435–6440.
- (18) Yu, J.; Hai, Y.; Cheng, B. Enhanced Photocatalytic H₂-Production Activity of TiO₂ by Ni(OH)₂ Cluster Modification. *J. Phys. Chem. C* **2011**, *115*, 4953–4958.
- (19) Dinh, C.-T.; Nguyen, T.-D.; Kleitz, F.; Do, T.-O. A new route to size and population control of silver clusters on colloidal TiO₂ nanocrystals. *ACS Appl. Mater. Interfaces* **2011**, *3*, 2228–34.
- (20) Joo, J.; Kwon, S. G.; Yu, T.; Cho, M.; Lee, J.; Yoon, J.; Hyeon, T. Large-scale synthesis of TiO₂ nanorods via nonhydrolytic sol-gel ester elimination reaction and their application to photocatalytic inactivation of *E. coli*. *J. Phys. Chem. B* **2005**, *109*, 15297–302.
- (21) Li, X.-L.; Peng, Q.; Yi, J.-X.; Wang, X.; Li, Y. Near monodisperse TiO₂ nanoparticles and nanorods. *Chem.—Eur. J.* **2006**, *12*, 2383–91.
- (22) Limaye, M. V.; Singh, S. B.; Date, S. K.; Kothari, D.; Reddy, V. R.; Gupta, A.; Sathe, V.; Choudhary, R. J.; Kulkarni, S. K. High

coercivity of oleic acid capped CoFe_2O_4 nanoparticles at room temperature. *J. Phys. Chem. B* **2009**, *113*, 9070–6.

(23) Sing, K. S. W.; Everett, D. H. W.; Haul, R. A.; Moscou, L.; Pierotti, J.; Rouquerol, J.; Siemieniowska, T. International Union Of Pure Commission On Colloid And Surface Chemistry Including Catalysis * Reporting Physisorption Data For Gas/Solid Systems With Special Reference To The Determination Of Surface Area And Porosity. *Pure Appl. Chem.* **1985**, *57*, 603–619.

(24) Qian, S.; Wang, C.; Liu, W.; Zhu, Y.; Yao, W.; Lu, X. An enhanced CdS/TiO_2 photocatalyst with high stability and activity: Effect of mesoporous substrate and bifunctional linking molecule. *J. Mater. Chem.* **2011**, *21*, 4945.

(25) Hu, H.; Kung, S.-C.; Yang, L.-M.; Nicho, M. E.; Penner, R. M. Photovoltaic devices based on electrochemical–chemical deposited CdS and poly(3-octylthiophene) thin films. *Sol. Energy Mater. Sol. Cells* **2009**, *93*, 51–54.

(26) Hotovy, I.; Huran, J.; Kobzev, A. P. Deposition and properties of nickel oxide films produced by DC reactive magnetron sputtering †. *Vacuum* **1998**, *51*, 157–160.

(27) Hotovy, I.; Huran, J.; Spiess, L.; Hascik, S.; Rehacek, V. Preparation of nickel oxide thin films for gas sensors applications. *Sens. Actuators, B* **1999**, *57*, 147–152.

(28) Zhu, H.; Yang, B.; Xu, J.; Fu, Z.; Wen, M.; Guo, T.; Fu, S.; Zuo, J.; Zhang, S. Construction of Z-scheme type $\text{CdS}-\text{Au}-\text{TiO}_2$ hollow nanorod arrays with enhanced photocatalytic activity. *Appl. Catal. B Environ.* **2009**, *90*, 463–469.

(29) Sabah, A.; Siddiqi, S. A.; Ali, S. Fabrication and Characterization of CdS Nanoparticles Annealed by using Different Radiations. *World Acad. Sci. Eng. Tech.* **2010**, *45*, 82–89.

(30) Dong, A.; Ye, X.; Chen, J.; Kang, Y.; Gordon, T.; Kikkawa, J. M.; Murray, C. B. A generalized ligand-exchange strategy enabling sequential surface functionalization of colloidal nanocrystals. *J. Am. Chem. Soc.* **2011**, *133*, 998–1006.

(31) Bao, N.; Shen, L.; Takata, T.; Domen, K. Self-Templated Synthesis of Nanoporous CdS Nanostructures for Highly Efficient Photocatalytic Hydrogen Production under Visible Light. *Chem. Mater.* **2008**, *20*, 110–117.

(32) Ma, G.; Yan, H.; Shi, J.; Zong, X.; Lei, Z.; Li, C. Direct splitting of H_2S into H_2 and S on CdS -based photocatalyst under visible light irradiation. *J. Catal.* **2008**, *260*, 134–140.

(33) Amirav, L.; Alivisatos, A. P. Photocatalytic Hydrogen Production with Tunable Nanorod Heterostructures. *J. Phys. Chem. Lett.* **2010**, *1*, 1051–1054.

(34) Ran, J.; Yu, J.; Jaroniec, M. $\text{Ni}(\text{OH})_2$ modified CdS nanorods for highly efficient visible-light-driven photocatalytic H_2 generation. *Green Chem.* **2011**, *13*, 2708.

(35) Sakai, N.; Ebina, Y.; Takada, K.; Sasaki, T. Electronic band structure of titania semiconductor nanosheets revealed by electrochemical and photoelectrochemical studies. *J. Am. Chem. Soc.* **2004**, *126*, 5851–8.

(36) Qi, L.; Yu, J.; Jaroniec, M. Preparation and enhanced visible-light photocatalytic H_2 -production activity of CdS -sensitized Pt/TiO_2 nanosheets with exposed (001) facets. *Phys. Chem. Chem. Phys.* **2011**, *13*, 8915.

(37) Meissner, D.; Memming, R.; Shuben, L.; Yesodharan, S.; Grätzel, M. Photocorrosion by Oxygen Uptake in Aqueous Cadmium Sulphide Suspensions. *Ber. Bunsenges. Phys. Chem.* **1985**, *89*, 121–124.

(38) Davis, A. P.; Huang, C. P. The removal of substituted phenols by a photocatalytic oxidation process with cadmium sulfide. *Wat. Res.* **1990**, *24*, 543–550.

(39) Weller, H.; Haase, M.; Spanhel, L.; Henglein, A. Charge carrier dynamics in colloidal semiconductors. *Prog. Colloid Polym. Sci.* **1988**, *76*, 24–26.